Int. J. Electrochem. Sci., 14 **(2019)** 1248 – 1269, doi: 10.20964/2019.02.44

International Journal of ELECTROCHEMICAL SCIENCE
www.electrochemsci.org

Novel approach to fabrication of DNA Biosensor Based on a Carboxylated Graphene Oxide Decorated with Fe_3O_4 NPs for the Detection of Typhoidal Salmonella

Shichao Xu[1,2,3,], Hao Duo[1], Chunming Zheng[1,2], Shihuai Zhao[1,2], Shidong Song[1,2], Gabriel Simon[4]*

[1] School of Environmental and Chemical Engineering, Tianjin Polytechnic University, 399 Binshui West Road, Tianjin 300387, China
[2] State Key Laboratory of Hollow Fiber Membrane Materials and Membrane Process, Tianjin Polytechnic University, 399 Binshui West Road, Tianjin 300387, China
[3] Tianjin Engineering Center for Safety Evaluation of Water Quality & Safeguards Technology Tianjin Polytechnic University, 399 Binshui West Road, Tianjin, 300387, China
[4] 18, rue du 8 mai 194549180, St Barthelemy d'Anjou Cedex, Esaip, France
[*]E-mail: xushichao@tjpu.edu.cn

Received: 5 October 2018 / *Accepted:* 27 November 2018 / *Published:* 5 January 2019

Diseases caused by typhoidal salmonella have led to a wide range of panic. It is thereby critically urgent to develop high-efficiency, ultrasensitive techniques for typhoidal salmonella detection. Carboxylated graphene oxide (CGO), features as one of the most crucial substrates to immobilize probe DNA for the fabrication of DNA biosensor, has been studied extensively so far. However, the reagents involved in the protocols proposed previously due to their strong alkalinity and extremely high reducing properties would impose significant impact to their performance and application. Herein, we develop a novel strategy for effective carboxylation graphene oxide with sodium citrate and chloroacetic acid. X-ray photoelectron spectroscopy (XPS) results demonstrate the density of carboxyl is improved more than twice, in consistent with the results of nuclear magnetic resonance (NMR). Furthermore, decorated with cost-effective Fe_3O_4 NPs, the conductivity of CGO could be enhanced remarkably, furthermore, far more 5'-end amino labeled probe DNA would be stably grafted. The performance of stepwise modification of the bioelectrodes is carried out by cyclic voltammetry (CV) and electrochemical impedance spectroscopes (EIS). Differential pulse voltammetry (DPV) studies exhibit a linear response ranging from 10^{-17} to 10^{-9} M for target DNA analysis with the detection limit up to 3.16×10^{-18} M, using methylene blue (MB) as a redox indicator under optimal conditions. In addition, the as-prepared biosensor provides predominant capability for discriminating the similar target DNA sequences. Eventually, the proposed biosensor is surveyed by real samples and it shows outstanding performance. Consequently, the developed ssDNA/Fe_3O_4 NPs/CGO/GCE can be a promising candidate for real patient samples analysis.

Keywords: Carboxylation; Graphene oxide; Fe_3O_4 nanoparticle; DNA biosensor; Typhoidal salmonella

1. INTRODUCTION

Salmonella isolates frequently cause human infection diseases from mild gastroenteritis to death, especially for the infants, the elderly, and immunocompromised hosts [1]. Salmonella is regarded as the riskiest bacteria owing to its extremely high rate of mortality (31%) among numerous bacterial pathogens that trigger foodborne diseases [2]. Typhoid fever, as one of the foodborne diseases caused by salmonella, is estimated to cause 12 million of cases worldwide annually and approximate 120000 deaths [3]. The organisms are often transmitted via the fecal-oral route and the diseases commonly attack in low/middle income countries such as south southeast Asia and subsaharan Africa due to poor quality of potable water, unhygienic living conditions and environments and improper sanitation system and utilities [4, 5]. Conventional and contemporary methods are only available at advanced stages of infections and suffering with numerous limitations[6]. Nevertheless, approaches of advanced molecular diagnosis techniques and immunological techniques, such as PCR, NASBA and ELIA require well-trained personnel and expensive equipments. Therefore, the development of facilities for accurate and immediate detection is of great importance for food safety and clinical diagnosis [7].

The vast achievements in nanomaterials and bioelectronics have made the development of various biosensors for the discrimination of a great deal of analytes possible, such as optical biosensors for the screening potential xenoestrogens and tumour necrosis factor-alpha [8,9], biosensor based on fluorescent for the detection of hydroquinone and glutathione [10, 11], and electrochemical nucleic acid-based biosensor for the detection of CYFRA21-1 and specific target DNA [12, 13]. Among them, electrochemical DNA biosensor takes advantage of strong specific binding between a probe DNA sequence and a certain target DNA fragment to produce electrochemical signal response transformation. Consequently, it offers the analytic results with higher reliability and selectivity, and meanwhile, the designed facilities possess the merit of miniaturization and reusability [14, 15].

To date, diversified electrochemical DNA biosensor have already been designed based on a broad range of nanomaterials such as gold nano-particle (GNA) [16], carbon nanotubes [17], graphene [18, 19], and miscellaneous noble metals to enhance the performance of DNA biosensors for the screen of l-cysteine and homocysteine [20] and breast cancer biomarkers diagnostic [21]. Among various nanomaterials, graphene provides immense active detection areas [22], much higher electron mobility and densities than semiconductors and metals [23], extremely high light transmittance ~98% [24], and excellent mechanical strength [25].

Graphene oxide (GO), a derivative of graphene, inherits most of the properties of graphene. In addition, GO can be modified extensively with presence of a variety of functional groups like -OH, -COOH, -CHO and -C=O. The reactive groups like carboxyl of GO often act as the anchor for the probe DNA assembly via the formation of amide to achieve covalent connection between the carboxyl and the probe DNA labeled with amino [26]. From this perspective, maximization the content of the carboxyl of GO can potentially enhance the number of immobilized probe DNA. As a result, the

sensitivity of the proposed biosensor can be improved.

Selective liquid-phase extraction have been reported with high yield of carboxyl-rich graphene oxide quantum dots [27]. A route was also designed to convert the other oxygen-containing functional groups of GO into the carboxyl [28]. However, these methods cannot be accomplished without using reagents like chloroform, hydrazine monohydrate. Alternatively, Hongjie Dai proposed an approach of carboxylation of GO [29, 30], which also suffers from the defect of being quick deoxygenation in the strong alkali conditions [31], so very limited amount of the carboxyl is obtained. Furthermore, studies have shown that the conductivity of GO decreases dramatically with the increase of oxidation degree. As a consequence, GO loaded with the other materials have aroused extensive interests, since the nanocomposites can vastly enhance the performance of GO. Fe_3O_4 NPs/GO composites due to its superiority of being easily collected, cost-effective and biocompatible have been utilized as drug carriers [32].

In this work, we design a novel protocol for effective carboxylation of GO for the first time, which greatly enhances the density of the carboxyl of GO and avoids the application of hypertoxic and risky reagents. Based on this strategy and deposited with low cost and facile fabrication of Fe_3O_4 NPs via electrostatic self-assembly, we propose a DNA biosensor aiming at the detection of typhoidal salmonella. The fabricated DNA biosensor exhibits the capability of achieving low detection limit of 3.16×10^{-18} M and broad dynamic detection range from 10^{-17} to 10^{-9} M. In addition, it offers outperformance for discrimination of the similar target DNA sequences by monitoring the oxidation peak of DPV using methylene blue as a redox indicator. When the constructed DNA biosensor is evaluated in the real serum samples, it displays the desirable analysing results.

2. EXPERIMENTAL

2.1. Materials and Apparatus

Sodium nitrate, potassium permanganate, graphite, hydrogen peroxide, ethylene glycol, hydrochloric acid, sodium acetate, chloroacetic acid, sulphuric acid, sodium citrate, nitric acid, sodium chloride, iron (III) chloride hexahydrate ($FeCl_3\cdot6H_2O$) were obtained from Tianjin Fengchuan Chemical Reagent Technologies Co. LTD (Tianjin, China). N-hydroxysuccinimide (NHS), Methylene blue (MB), ethylenediaminetetraacetic acid (EDTA), Tris(hydroxymethyl)-aminomethane (Tris-HCl), N-(3-dimethylamminopropyl)-N′-ethylcarbodiimide hydrochloride (EDC) were all purchased from Shanghai Aladdin Industrial Corporation Co. LTD (Shanghai, China). Human serum were purchased from People's Hospital of Tianjin. All reagents were of analytical grade without further purification. The DNA sequences used for biosensor preparation are as follows:

SsDNA Probe: 5′-NH_2-$(CH_2)_6$-CGTGCGCGACGCCCGCCGCC-3′

It is noteworthy that this DNA sequence does not match to any other related species of family Enterobacteriaceae and with other micro-organisms [33].

Target DNA sequence: 5′-GGCGGCGGGCGTCGCGCACG-3′

Non-complementary DNA sequence: 5′-GTAACCTGCCTGTAAGACTG-3′

One base mismatch DNA sequence: 5′-GGCGCCGGGCGTCGCGCACG-3′

The DNA sequences above were purified by high performance liquid chromatography and supplied by Shanghai Invitrogen Biotechnology Co. LTD (Shanghai, China). Ultrapure water (18.2> MΩ cm^{-2} resistance) was used throughout the experiment. Tris-HCl buffer solution (50 mM,Tris(hydroxymethyl)-aminomethane and 20 mM, NaCl, pH=7.4). 2×SSC buffer solution (0.3 M NaCl and 0.03 M tris-sodium citrate). TE buffer solution (10 mM Tris-HCl, 1mM EDTA, pH=7.4). Phosphate buffer 0.1 M NaH_2PO_4 and 0.1 M Na_2HPO_4 [v(Na_2HPO_4):v (KH_2PO_4)=8:2, tris-HCl buffer (50 mM Tris-HCl, 20 mM NaCl, pH=7.4).

Fourier transform infrared (FTIR) spectrum was collected by fourier infrared spectrometer (Thermo Fisher, Nicolet 6700, USA). X-ray photoelectron spectroscopy (XPS) was recorded using an X-ray photoelectron spectrometer (PHI-5300, America). ^1H of nuclear magnetic resomance (NMR) spectroscopy was recorded by nuclear magnetic resomance spectrometer (Bruke, Advanced III HD, Germany). Scan electron microscopy (SEM) micrographs were carried out using a sigma300 (ZEISS, Germany). Electrochemical signal was collected by ParStat 4000 electrochemistry workstation (AMETEK, USA).

2.2. Preparation of CGO

GO was synthesized according to a modified Hummers method [34]. Briefly, 2 g sodium nitrate and 3 g potassium permanganate were dissolved in 92 mL of 98% sulfuric acid in an ice bath with constant stirring. Subsequently, 2 g graphite powder was slowly added with vigorous agitation in case of sudden increase of temperature. Afterward, the mixture was transferred to a 35 ℃ water bath and kept continuous stirring for 1h. Then 192 mL of ultrapure water was gradually added in the mixture and then the temperature of the mixture was increased to 95 ℃ and also kept for 15 min. With the oxidation of graphite, the solution became aureate slowly. Whereafter, 30% H_2O_2 was added with caution in order to eliminate excessive potassium permanganate. After being set aside for several hours, the supernatant of the solution was removed carefully, and the product was washed with sufficiently 5% hydrochloric acid and ultrapure water, respectively. Finally, the desirable product was dialyzed for two days and dried under vaccum.

16 g chloroacetic acid was added into an aqueous suspension of 2 mg mL^{-1}, 80 mL GO. Subsequently, 16.6 g tris-sodium citrate was dispersed uniformly in the mixture, and then the solution was sonicated for 1h to assure the reaction can be accomplished totally. Eventually, the suspension was purified by dialysis at room temperature for two days to obtain the resultant which was dried under frozen and vacuum conditions.

2.3. Preparation of Fe_3O_4 NPs/CGO

Fe_3O_4 NPs were synthesized on the basis of the hydrothermal method [35]. In brief, 1.35 g of $FeCl_3 \cdot 6H_2O$ was dissolved by 40 mL of ethylene glycol with constant mechanical stirring until a uniform solution was observed. Then NaAc of 3.6 g was added. After being sonicated for 30 min the mixture was kept for 9 h at 200 ℃. Subsequently, a black product was obtained and collected with a

magnet. The product was finally washed by absolute ethanol for three times to remove the impurities before being dried in the oven under vacuum condition.

Fe_3O_4 NPs with a positively charged surface were prepared by dispersing Fe_3O_4 NPs in 1 M HNO_3 [36]. Then 10 mg positively charged Fe_3O_4 NPs were added to 1 mg ml^{-1}, 10 ml CGO suspension. After constant stirring of the mixture for 5 h, a homogeneous suspension was obtained. The resulting nanocomposites were collected by applying an external magnetic field for several hours to collect the precipitate. The nanomaterials were ultimately dried under the frozen and vacuum conditions. Finally, we obtained Fe_3O_4 NPs/CGO. Similarly, Fe_3O_4 NPs/GO, Fe_3O_4 NPs@GO (without being treated by HNO_3) were prepared as well.

2.4. Fabrication of the ssDNA/Fe_3O_4 NPs/CGO/GCE

Pretreatment of the glassy carbon electrode (GCE) was operated as follows. A 3 mm diameter GCE was polished successively with 0.3 μm and 0.05 μm alumina slurry to a mirror-like surface. Subsequently, it was sonicated in ultrapure water, ethanol and ultrapure water for 5 min, respectively. And then it was electrochemically cleaned in 0.50 M H_2SO_4 using a repetitive cyclic potential scanning for 20 cycles from -0.3 to +1.50 V with a scan rate of 100 mV s^{-1} to remove any possible residuals. It was finally sonicated for five minutes in ultrapure water and dried in the flow of nitrogen. 10 μL, 1 mg ml^{-1} prepared Fe_3O_4 NPs/CGO solution was coated on the clean GCE and dried at room temperature for 24 h to obtain the modified electrode, which is denoted as Fe_3O_4 NPs/CGO/GCE. Subsequently, 10 μL tris-HCl buffer (containing 25 mM EDC and 10 mM NHS) was dropped on the surface of Fe_3O_4 NPs/CGO/GCE at 25 ^oC and incubated for 1 h. After being washed by tris-HCl buffer and ultrapure water, 10 μL amino-labeled probe DNA was deposited onto the Fe_3O_4 NPs/CGO/GCE surface and incubated for 1 h. Finally, the functionalized electrode was followed by rinsing with 10 μL tris-HCl buffer and ultrapure water to remove unbound ssDNA. The biosensor was denoted as ssDNA/Fe_3O_4 NPs/CGO/GCE. Via the similar procedures of treatment, the bioelectrode of ssDNA/Fe_3O_4 NPs/GO/GCE was also obtained.

2.5. Optimization of assay conditions

Experimental conditions for DNA hybridization were optimized by EIS. Initially, the hybridization temperature was fixed at 30 ^oC and recorded the curves of EIS ranging from 20 to 60 min. Then the hybrizating incubation time was kept at 50 min to record the EIS diagram imposed by temperature ranging from 15 to 35 ^oC. The concentration of target DNA were 10^{-9} M both used in the process.

Each of the bioelectrodes was tested in Zobell's solution (5 mM $K_3[Fe(CN)_6]$ and 5 mM $K_4[Fe(CN)_6]$, containing 0.1 mol L^{-1} KCl) at the potential of 0.17 V and within the frequency ranging from 0.01 to 100000 Hz using an AC amplitude of 5 mV, Zobell's solution was harnessed to probe the impedance of a modified electrode surface.

2.6. Sensitivity for target detection

Sensitivity verifications were carried out by immersing biosensors of probe DNA/Fe_3O_4 NPs/CGO/GCE into 2×SSC buffer solution containing various concentrations of target DNA at 30 ℃ for 50 min. The hybridized bioelectrodes were rinsed with 50 tris-HCl buffer to remove the extra target DNA. Subsequently, the hybridized bioelectrodes of dsDNA/Fe_3O_4 NPs/CGO/GCE were further immersed into Tris-HCl buffer containing 10 μM MB and 20 mM NaCl for 5 min with continuous stirring. The hybridized DNA biosensors were denoted as dsDNA/Fe_3O_4 NPs/CGO/GCE. DPV curves were measured in phosphate buffer from -0.55 to 0.1 V, with the pulse height of 50 mV, step height of 25 mV, step width of 0.05 s and pulse width 0.005 s. The procedures for the stepwise fabrications of the biosensor were illustrated in Fig. 1.

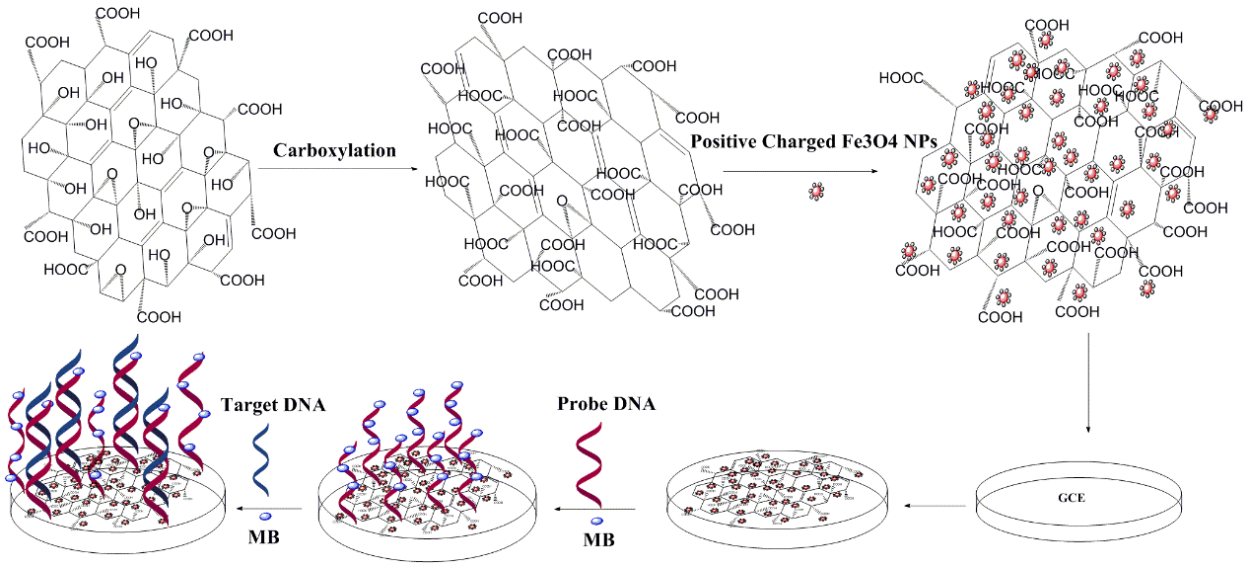

Figure 1. Schematic diagram of the assembly process of the working electrode.

3. RESULTS AND DISCUSSION

3.1 Morphology and characterization of GO, CGO, Fe_3O_4 NPs/GO, Fe_3O_4 NPs/CGO

There are typical crumpled and wrinkled regions of GO in Fig. 2A, indicating that graphite has been oxidized into graphene oxide. Much more wrinkle domains are observed in CGO (Fig. 2C) than GO, which could be contributed to carboxylation process. It can also be observed from the SEM images of Fe_3O_4 NPs/GO (Fig. 2B) and Fe_3O_4 NPs/CGO (Fig. 2D), the Fe_3O_4 NPs have been absorbed onto the surface of GO and CGO successfully by electrostatic self-assembly, moreover, compared to the Fe_3O_4 NPs/GO, the Fe_3O_4 NPs are wrapped more closely by CGO.

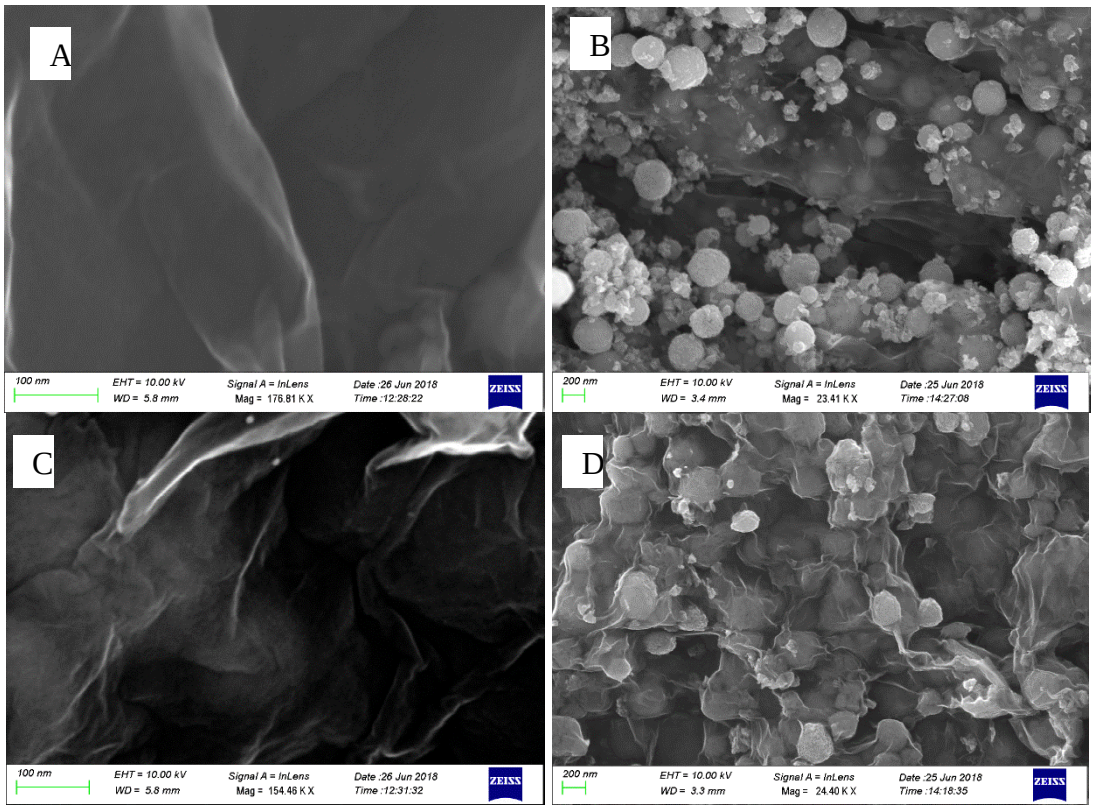

Figure 2. SEM images of (A) GO, (B) Fe_3O_4 NPs/GO, (C) CGO, (D) Fe_3O_4 NPs/CGO.

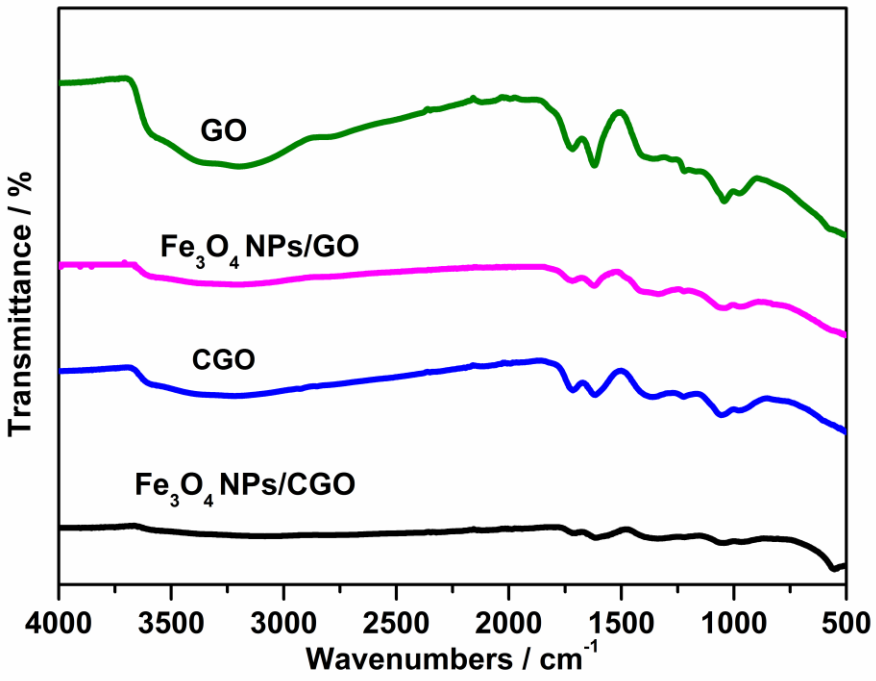

Figure 3. FTIR spectra of GO, Fe_3O_4/GO, CGO, Fe_3O_4/CGO.

As shown in Fig. 3. FTIR is employed to characterize GO, CGO, Fe_3O_4 NPs/GO and Fe_3O_4 NPs/CGO. A broad band is observed at ~ 3400 cm^{-1} , which can be ascribed to the stretching vibrations of O-H, the peak at 1720 cm^{-1} is an indication of the C=O carboxylic acid groups [37], the aromatic C=C ring stretching can be observed at 1620 cm^{-1}, C-OH stretching vibrations in epoxy groups is at 1224 cm^{-1}, C-O stretching vibrations in carboxylic acid is at 1050 cm^{-1} [38]. Via being carboxylated by citric sodium and chloroacetic acid, it can be seen that CGO can retain all the functional groups exhibited in GO. After being decorated Fe_3O_4 NPs with GO and CGO, respectively, significant change occurs to each functional group, this could be attributed to the successful deposition of Fe_3O_4 NPs onto the surface of GO and CGO.

XPS is utilized to monitor the transformation of surface chemistries from GO to CGO as well as the changes of chemical composition triggered by the deposition of Fe_3O_4 NPs. In the Fig. 4A&B, via being deconvoluted, five main carbon bonds of C1 can be observed for GO and CGO. C=C at 284.6 eV and 284.8 eV are assigned to sp^2 hybrids. What's more, C-C at 285.5 eV and 285.4 eV are subject to sp^3 hybrids [39]. C-O is at 287.13 eV and 287.03 eV, C=O is at 288 eV and 288.23 eV, and O-C=O is at 288.97 eV and 289.1 eV, respectively. The percentage of the O-C=O in oxygen containing functional groups increases from 16.5% of GO to 38.3% of CGO and oxygen-containing functional groups in the whole groups only decrease 1.07% because of the carboxylation, which is indicative of effectively carboxylated GO. Eventually, as depicted in XPS curves of Fe 2p (Fig. 4C), peak of Fe_3O_4 NPs/CGO descends due to the carboxylation, which causes the elimination of fractional functional groups of GO nanosheet.

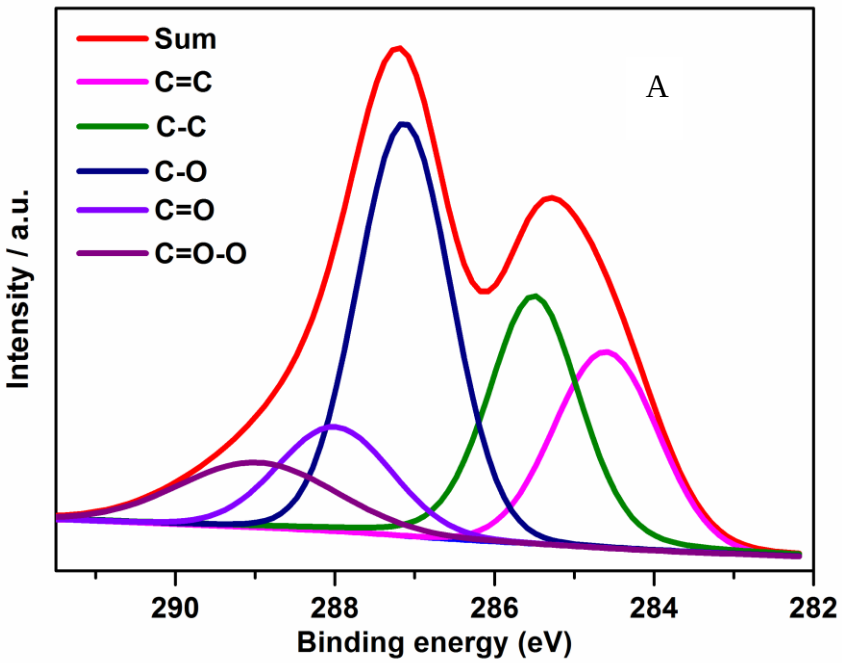

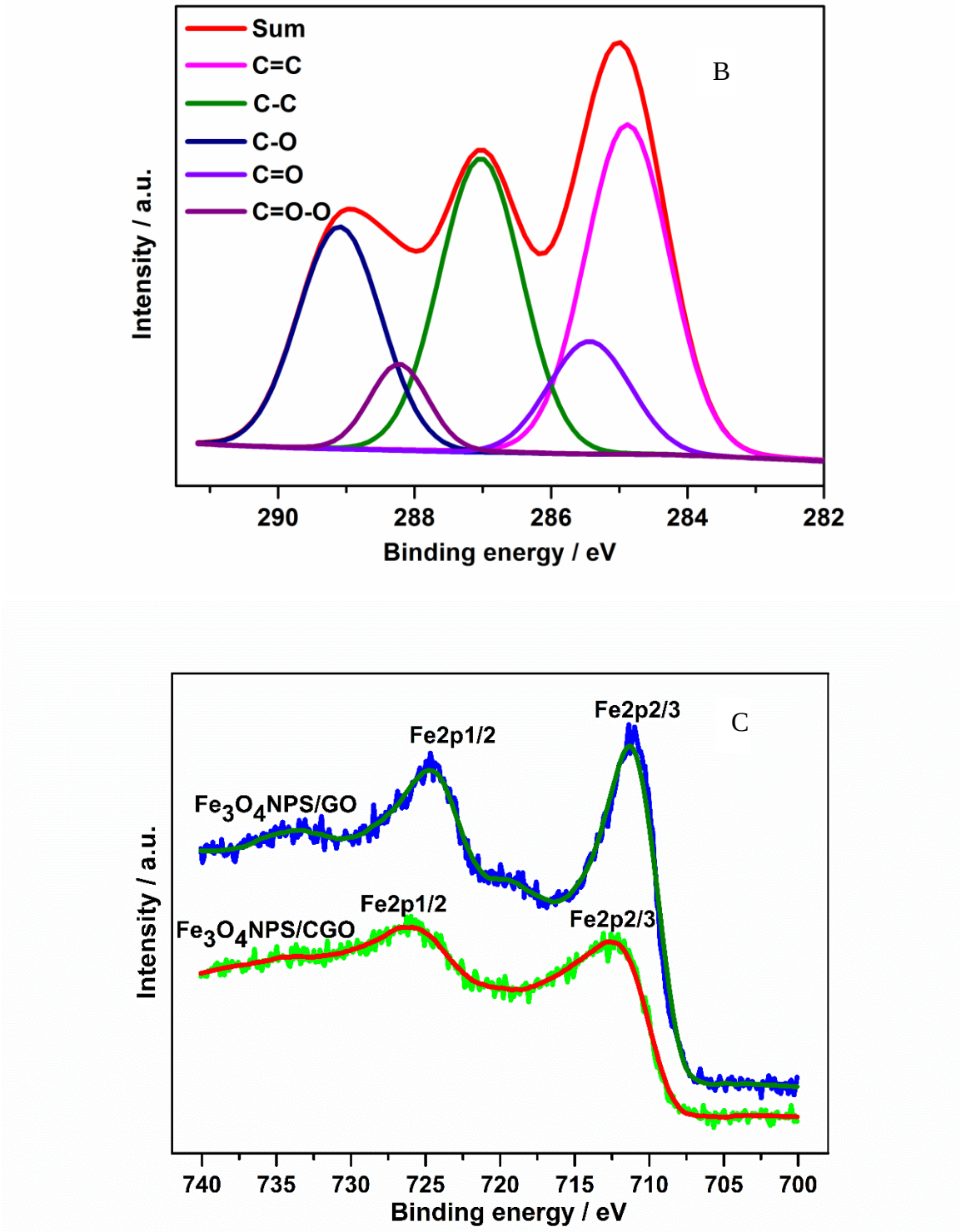

Figure 4. XPS spectra of (A) GO, (B) CGO, (C) Fe_3O_4 NPs/GO & Fe_3O_4 NPs/CGO.

NMR is an extremely powerful tool used to characterize functional groups. It is currently employed to confirm the structural transformation led by carboxylation. Although the carboxyl does exist on the surface of GO, their concentration is too low for NMR to detect [40], that is, no peak is found in the range of δ (9 to 13) in Fig. 5A. Whereas, a peak is observed at δ(11.7) in Fig. 5B, which is

caused by the increasing density of the carboxyl of CGO in agreeable with the conclusion obtained from XPS. Furthermore, δ(1.3), δ(2.5), δ(3.5) and δ(4.25) are attributed to the presence of R_3CH, HC-C=O, C-OH and H_2CR_2, respectively.

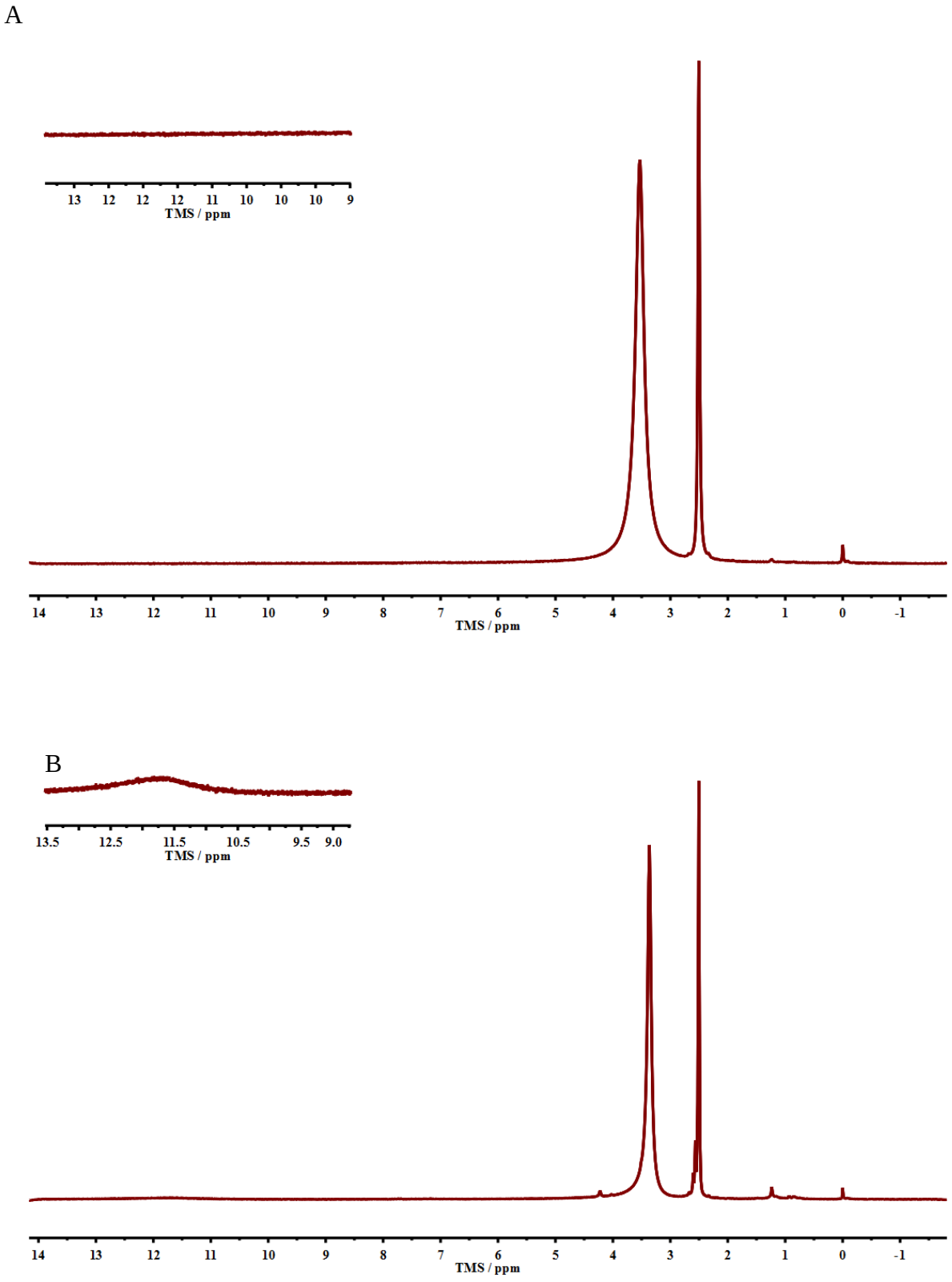

Figure 5. NMR spectra of (A) GO, (B) CGO.

3.2 Electrochemical characterization of the functionalized electrodes

CV is harnessed to probe the behavior of the GCE surface functionalized with various materials. As illustrated in Fig. 6, a pair of reversible redox peaks are observed, which can be attributed to $[Fe(CN)_6]^{3-/4-}$ transformation. The magnitude of the peak current increases in the order of GO/GCE, Fe_3O_4 NPs@CGO/GCE, Fe_3O_4 NPs/GO/GCE, CGO/GCE, Fe_3O_4 NPs/CGO/GCE and bare GCE. Bare GCE (a) manifests the highest peak current, owing to its excellent charge transfer capability. Whereas, since the repulsive interaction between the negatively charged [41] oxygen-containing functional groups of GO and the ions in the electrolyte, which results in the signal response of GO/GCE (f) reduces to the minimum. Fe_3O_4 NPs are used to neutralize the negatively charged capability of GO, and it is achieved via directly physical absorption (Fe_3O_4 NPs@GO, curve e) and electrostatic self-assembly (Fe_3O_4 NPs/GO, curve d).

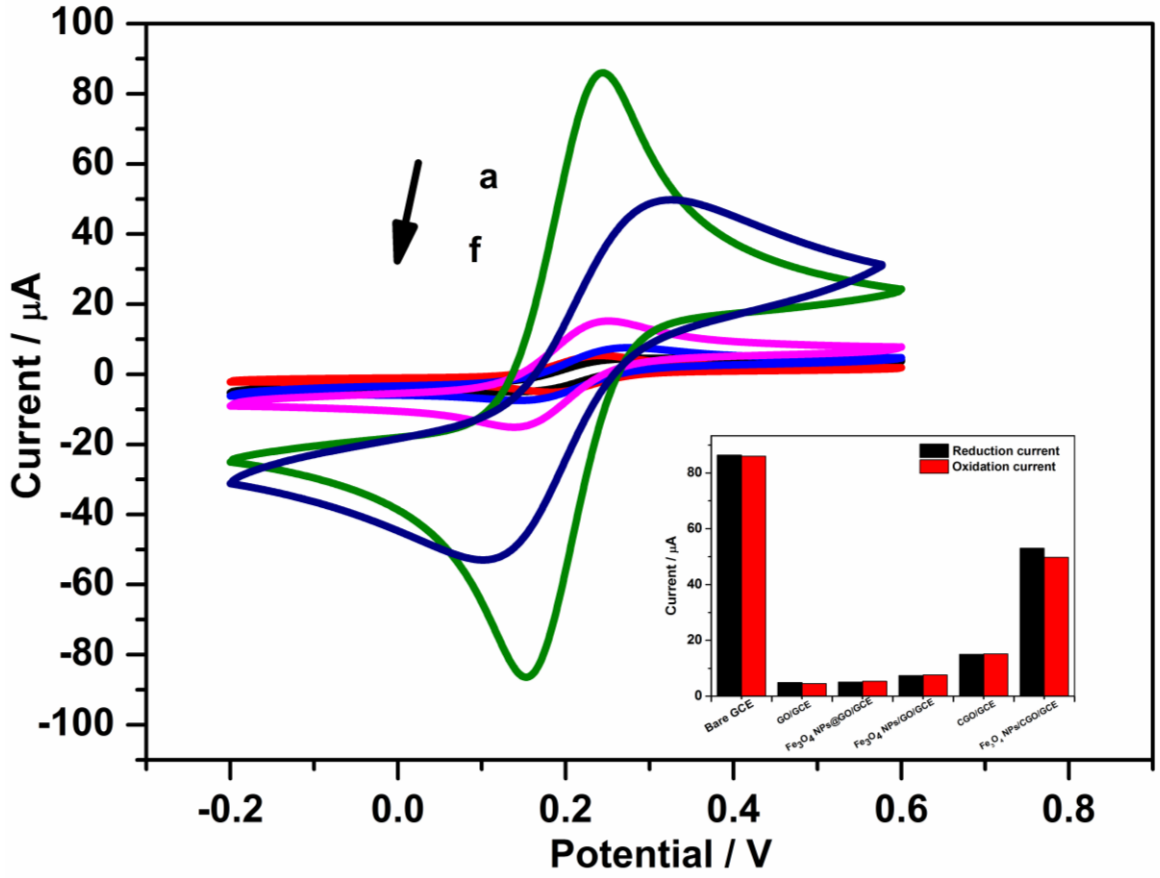

Figure 6. CV diagram of the GCE functionalized by various materials in 5 mM $[Fe(CN)_6]^{3-/4-}$ containing 0.1 M KCl solution at 50 mV s^{-1}, (a) bare electrode, (b) Fe_3O_4 NPs/CGO/GCE, (c) CGO/GCE, (d) Fe_3O_4 NPs/GO/GCE, (e) Fe_3O_4 NPs@GO/GCE, (f) GO/GCE. Inset shows oxidation current & reduction current of CV of the GCE functionalized by various materials.

Compared to the GO/GCE, almost negligible change appears in the Fe_3O_4 NPs@GO/GCE. Nevertheless, apparent increase occurs to the Fe_3O_4 NPs/GO/GCE, proving electrostatic self-assembly can provide more favorable conditions for Fe_3O_4 NPs to accelerate the electron transfer kinetic of

$[Fe(CN)_6]^{3-/4-}$. Despite slight reduction involves in the carboxylation procedure, CGO/GCE (c) can still exhibit even higher peak current than the Fe_3O_4 NPs/GO/GCE. Ultimately, after depositing with Fe_3O_4 NPs/CGO on the GCE (b), the impedance decreases dramatically, which is associated with the fact that reactive sites onto the electrode available for the transformation of $[Fe(CN)_6]^{3-/4-}$ increases. It can be assumed due to the diversity of structure, which causes the significant difference of electron transfer kinetics between Fe_3O_4 NPs/GO and Fe_3O_4 NPs/CGO.

Three-electrode system was harnessed by CV to probe the features of electrochemical behaviors on the interface of the electrode at various scan rates (0.02-0.16 V s^{-1}), as presented in Fig. 7A, the coupled redox peak currents increased with the scan rate, suggesting that the kinetics of the redox reaction was diffusion controlled [42]. What's more, Fig. 7B. revealed that anodic peak current (I_{pa}) and cathodic peak current (I_{pc}) increased linearly with square root of scan rate (Eq. (1) and Eq. (2)) having regression coefficient (R^2) 0.995 and 0.990 for I_{pa} and I_{pc}, respectively. Because of $\triangle E_p >$ 0.059V and $1.0 < I_{pa}/I_{pc} = 1.03 < 1.27$, indicating the quasi reversible reaction behavior occurred on the electrode surface[43, 44].

$$I_{pa} = 1.59637\times10^{-5}\nu^{1/2} + 1.30894\times10^{-4} \quad (1)$$

$$I_{pa} = -1.57561\times10^{-5}\nu^{1/2} - 1.35226\times10^{-4} \quad (2)$$

$$I_p = (2.69\times10^5)n^{3/2}AD^{1/2}C\nu^{1/2} \quad (3)$$

In the Eq. (3) of Randles-Sevick [45], Where I_p refers to the peak current, ν is scan rate in V s^{-1}, A is the surface area of the electrode (cm^2), C is the concentration of $K_3[Fe(CN)_6]$ (here $C=5\times10^{-6}$ mol cm^{-3}), n is the number of electrons transferred (here n=1), 'D' was calculated to be 7.73×10^{-5} cm s^{-1}.

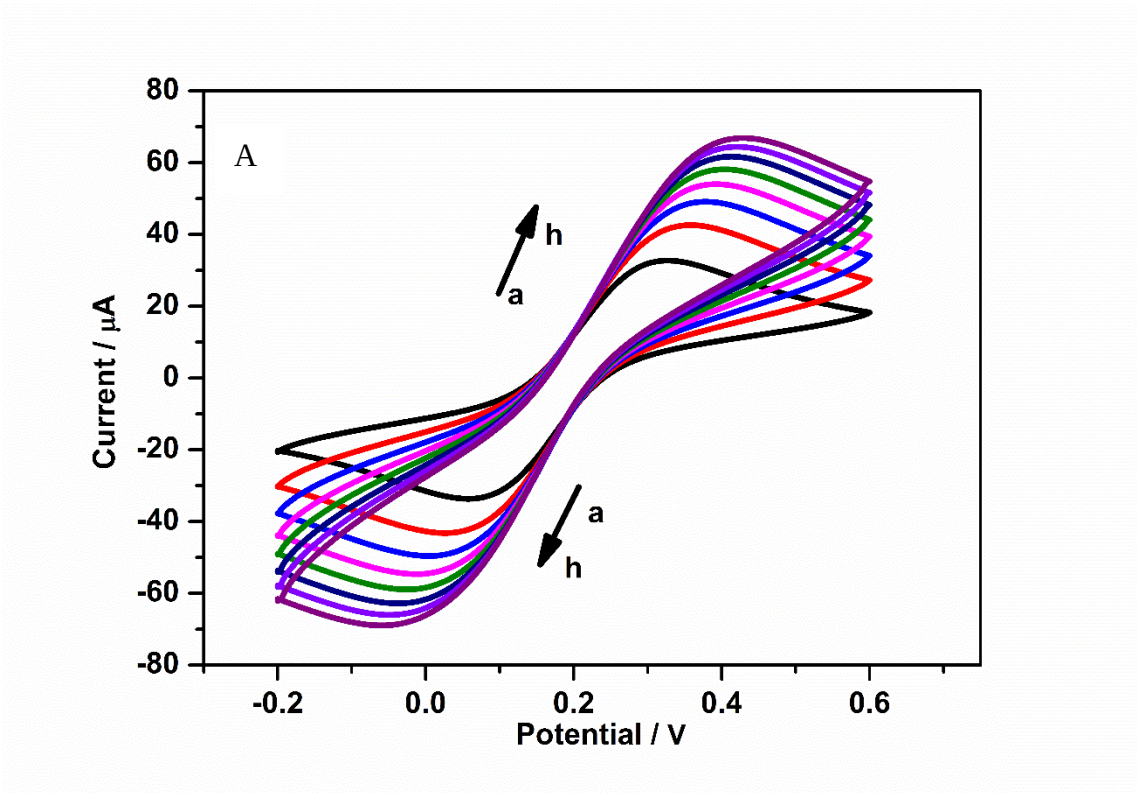

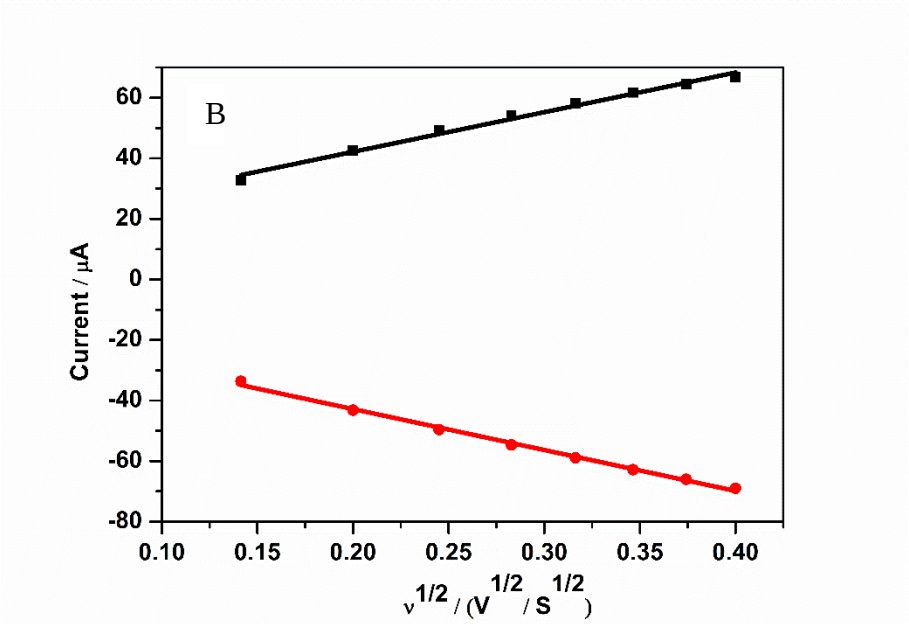

Figure 7. Cyclic voltammograms of (A) in 5 ×10^{-3} mol L^{-1} $Fe(CN)_6^{3-/4-}$ with 0.1 mol L^{-1} KCl at 0.02-0.16 V s^{-1}. (B) Plot of peak current vs. square root of the scan rate.

3.3 Characterization of the functionalized bioelectrodes

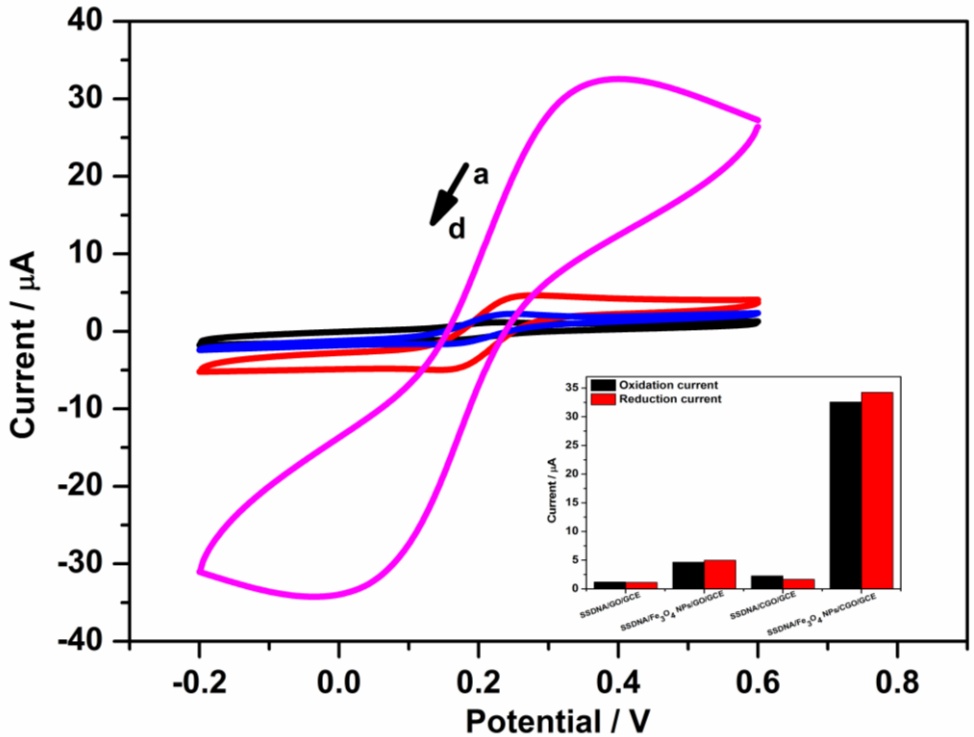

Figure 8. Cyclic voltammograms of the GCE functionalized with various materials and graft with probe DNA, respectively, in 5 mM $[Fe(CN)_6]^{3-/4-}$ containing 0.1 M KCl solutions at the scan rate of 50 mV s^{-1}. (a) ssDNA/Fe_3O_4 NPs/CGO/GCE, (b) ssDNA/Fe_3O_4 NPs/GO/GCE, (c) ssDNA/CGO/GCE, (d) ssDNA/GO/GCE. Inset shows oxidation current & reduction current of CV of the functionalized bioelectrodes.

Being attached with probe DNA on the Fe_3O_4 NPs/CGO/GCE, Fe_3O_4 NPs/GO/GCE, CGO/GCE and GO/GCE, respectively, compared to Fig. 6, each oxidation current & reduction current of them in Fig. 8 decreases which can be ascribed to the repulsion between phosphate backbone of probe DNA and the negatively charged ions of $[Fe(CN)_6]^{3-/4-}$ [46]. Exceptionally, the conductivity of the CGO/GCE overpasses the Fe_3O_4 NPs/GO/GCE in Fig. 6. However, since the remarkably increased density of the assembled probe DNA onto CGO/GCE than Fe_3O_4 NPs/GO/GCE, which significantly decreases the electron transfer kinetics of $[Fe(CN)_6]^{3-/4-}$, consequently, the situation becomes inversely in Fig. 8. Eventually, being attached probe DNA to the Fe_3O_4 NPs/CGO/GCE, since Fe_3O_4 NPs immobilized via electrostatic self-assembly can greatly facilitate the electron transfer kinetics, thus tremendous increase of conductivity of the ssDNA/Fe_3O_4 NPs/CGO/GCE is observed.

EIS due to its innet merits of label-free and non-destructive [47], thus it is further employed to confirm the results obtained from CV. In the present study, $[Fe(CN)_6]^{3-/4-}$ is used as the redox probe [48], as shown in Fig. 9. The diameter of the semicircle in EIS is equivalent to charge transfer resistance (R_{ct}). Inset shows the equivalent circuit of EIS. R_S reflects the electrolyte resistance. R_{ct} stands for the charge transfer resistance. CPE and W represent the double layer capacitance and Warburg impedance, respecitively. In the modification process of the electrode, the R_S, CPE and W show no regular change, the change of R_{ct} manifests the variation of the electron transfer resistance [49].

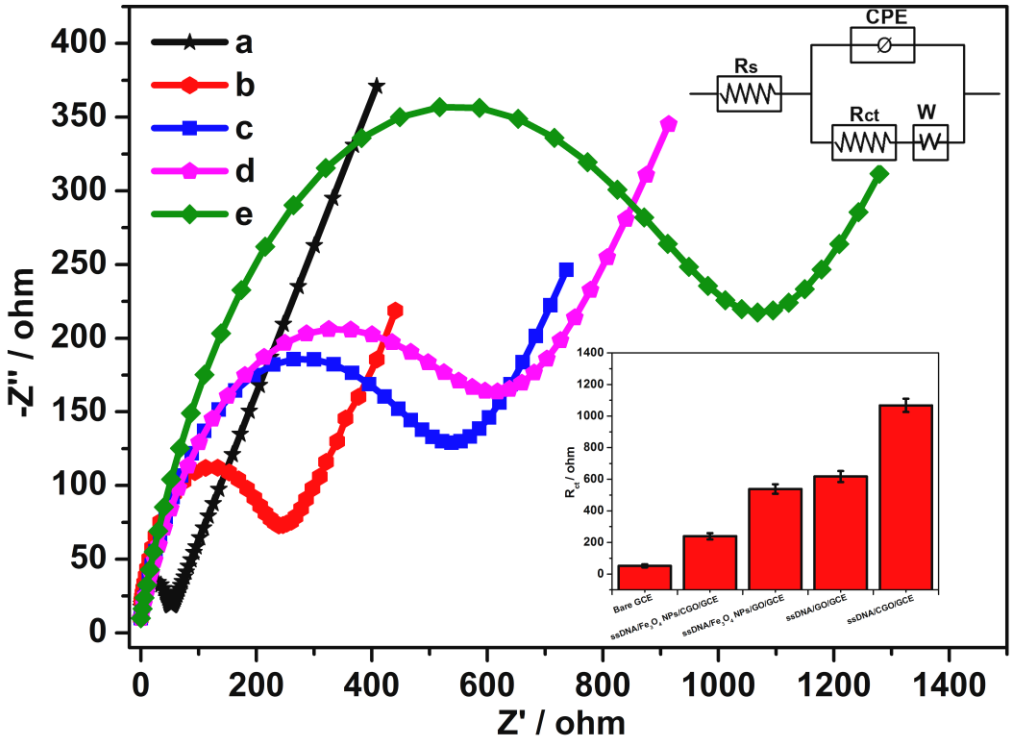

Figure 9. Nyquist diagram of different modifications of the GCE grafted with probe DNA (a) Bare GCE, (b) ssDNA/Fe_3O_4 NPs/CGO/GCE, (c) ssDNA/Fe_3O_4 NPs/GO/GCE, (d) ssDNA/GO/GCE, (e) ssDNA/CGO/GCE

As illustrated in curve a, the bare GCE shows the minimum semicircle domain (51.9 Ω), suggesting an excellent charge transfer process. The bioelectrode of ssDNA/GO/GCE (curve d) reveals largely increased charge transfer resistance (617.5 Ω), indicating the anionic $[Fe(CN)_6]^{3-/4-}$ is blocked to access the active centers by the phosphate backbone of DNA as well as oxygen-containing functional groups of GO. Subsequently, the R_{ct} ssDNA/Fe_3O_4 NPs/GO/GCE displays a small quantity of decrease (538.1 Ω), which indicates Fe_3O_4 NPs immobilized by electrostatic self-assembly can promote the electron transfer kinetics. Furthermore, as shown in curve e, the bioelectrode of ssDNA/CGO/GCE possesses the highest value of R_{ct} (1067.8 Ω), which suggests the greatly increased density of grafted DNA could dramatically enhance the charge transfer resistance. Eventually, the R_{ct} of the biosensor of ssDNA/Fe_3O_4 NPs/CGO/GCE reduces distinctly (239.1 Ω), which could be considered that the negatively charged capacity of the bioelectrode of the ssDNA/CGO/GCE is greatly weakened by Fe_3O_4 NPs.

3.4 Optimization of the experimental conditions

As it is well known that hybridization time and temperature play vital role in the hybridizating efficiency of the DNA biosensors, consequently, to achieve superior analytical performance of the proposed strategy, the experimental conditions including time and temperature for the hybridization are optimized. Presently, EIS is used to monitor the hybridization. In Fig. 10A, it is obvious that the value of R_{ct} reaches a plateau, when the time is beyond 50 min.

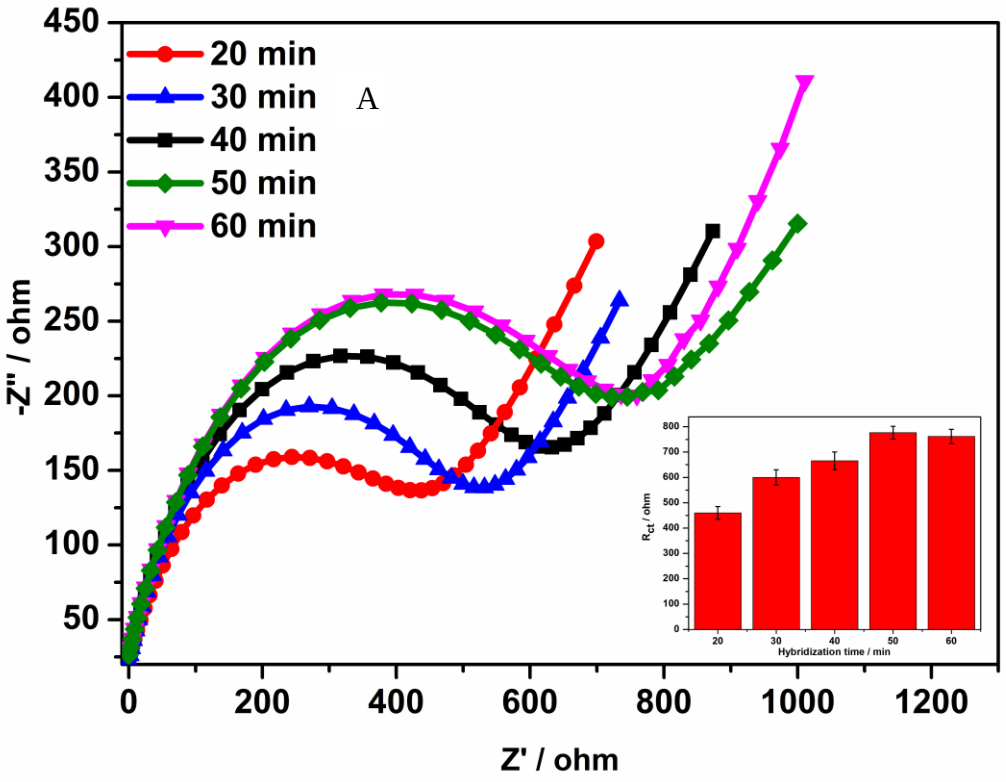

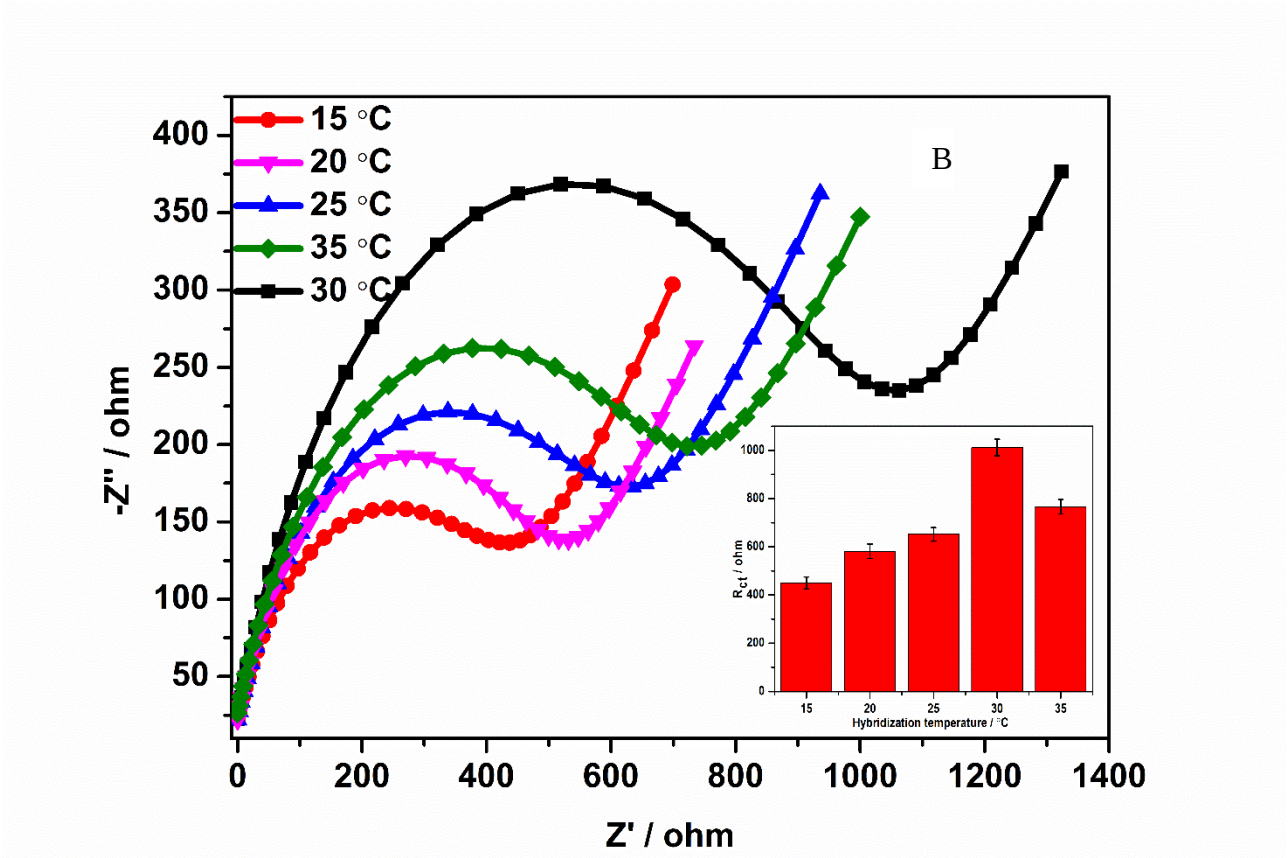

Figure 10. Nyquist plots of different hybridization time and temperature of (A) and (B), respectively, in zobell's solution, from 0.01 to 100000 Hz with signal amplitude of 5 mV at the potential of 0.17 V. Inset (A)&(B) of the plot graph of incubation time and temperature vs. R_{ct} value in (A)&(B).

Therefore, 50 min is chosen as a more economic hybridization temperature. In the range of 15-35 ℃, as depicted in Fig. 10B, the value of R_{ct} increases with the temperature from 15 to 30 ℃. As the temperature comes to 35 ℃, a sharpe decline is observed. As a consequence, 35 ℃ is selected as a more conducive temperature to complete the hybridization process.

3.5 Senstivity investigation of the fabricated DNA biosensor

Fig. 11 demonstrates DPV response of ssDNA/Fe_3O_4 NPs/CGO biosensor is applied to examine the event of hybridization with various concentration of target DNA sequences using MB as a hybridization indicator. Due to the different affinities of MB to ssDNA and dsDNA, MB is generally used as an electrochemical indicator to study the DNA hybridization. Indeed, MB has a strong affinity for free guanine bases [50]. Compared with dsDNA, it has a higher affinity for ssDNA, leading to decrease of peak current after the hybridization.

The analytical performance of the constructed biosensor is studied within the optimized conditions. As exhibited in inset of Fig. 11 inset, the response of DPV increases linearly with the logarithm of target DNA concentration ranging from 10^{-9} to 10^{-17} M and the corresponding regression

equation is I(μA)=36.37+1.92×log [C(M)] with the correlation coefficient of 0.9980. The limit of the detection is obtained with 3.16×10^{-18} M (signal/noise ratio of 3).

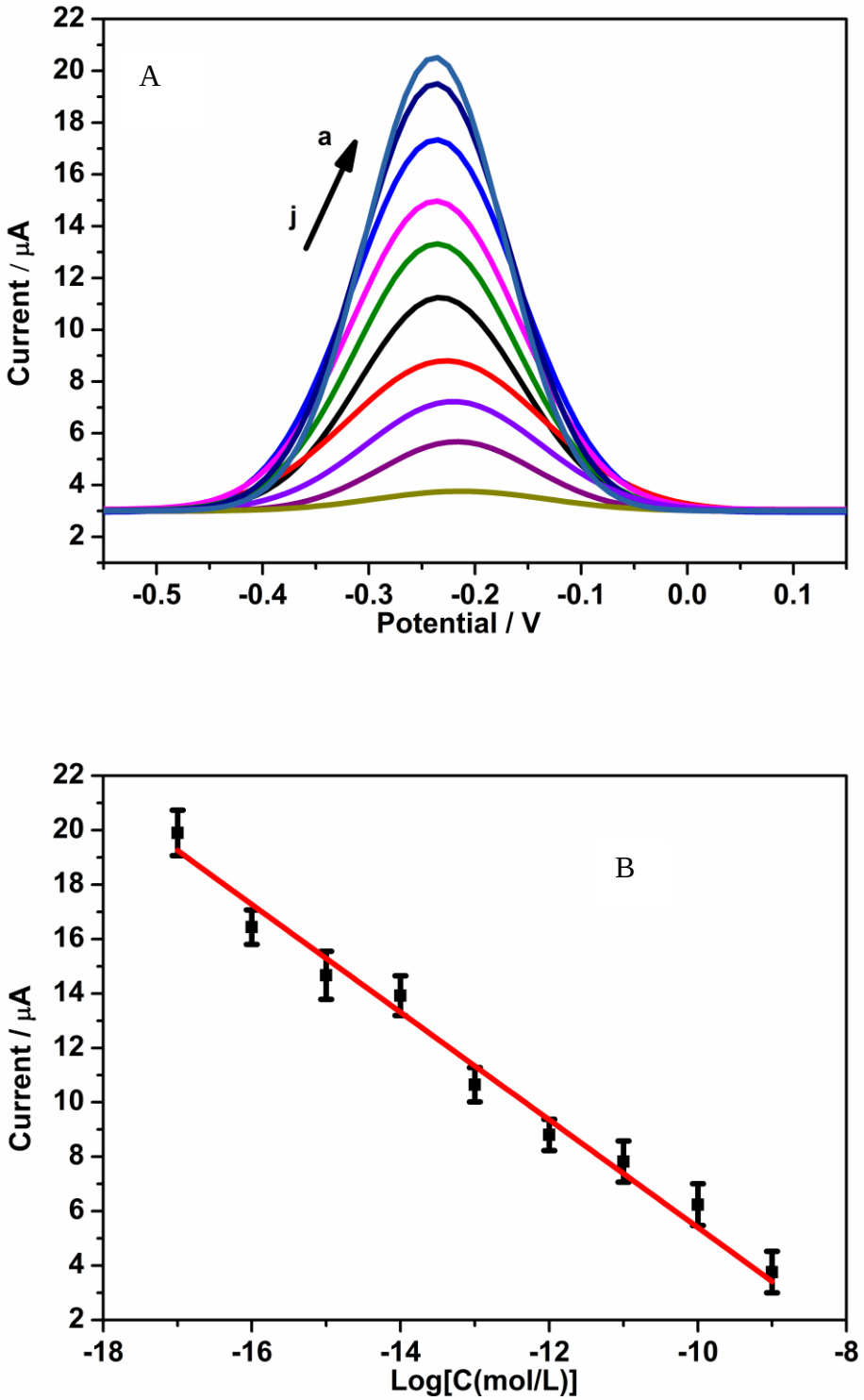

Figure 11. (A)DPV curves under optimal conditions after hybridization with 0 M, 10 aM, 0.1 fM, 1 fM, 10 fM, 0.1 pM, 1 pM, 10 pM, 0.1 nM and 1 nM target DNA (curves a-j, respectively). (B) shows plot of peak current vs. Log of the concentration of target ssDNA in PBS (0.1 mol L^{-1} , pH= 7.2) with MB as a redox indicator.

Table I. Comparison table for the Salmonella detection based on DNA biosensors.

Modified electrode	DNA probe sequences (5'→3')	Linear range (M)	Detection limit (M)	References
Polystyrene /GCE	TAG TAG CTC AGA ATA	5.7×10^{-7}-8.0×10^{-7}	5.5×10^{-7}	[51]
Nanoporous GCE	GGA GCT GCT GGC ATT ATT GAA	1×10^{-12}-400×10^{-12}	0.15×10^{-12}	[52]
GO/Chitosan/GCE	CGT GCG CGA CGC CCG CCG CC	10×10^{-15}-50×10^{-9}	10×10^{-15}	[53]
Fe_3O_4 NPs/CGO/GCE	CGT GCG CGA CGC CCG CCG CC	1×10^{-17}-1×10^{-9}	3.16×10^{-18}	This work

Compared to the other biosensors developed previously (listed in Table I.) for the detection of salmonella, this biosensor possesses a good performance of providing a broader linear range and a lower detection limit.

3.6 Analytical performance of the biosensor

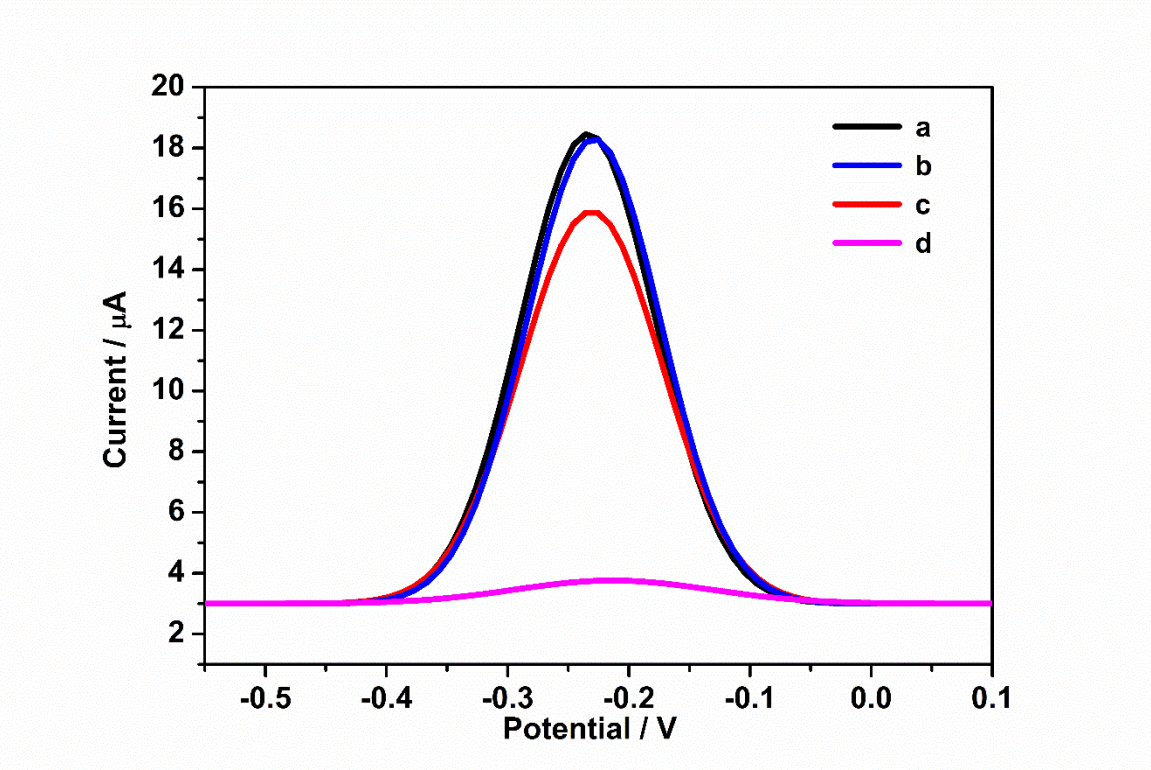

Figure 12. DPV response curves for bioelectrode of ssDNA/Fe_3O_4 NPs/CGO/GCE and the bioelectrode treated with non complementary, one base mismatch and complementary target DNA, 1nM each (Curve a, b, c, d, respectively).

In order to have a insight about the selectivity of the biosensor, DPV is also employed to investigate the ssDNA/Fe_3O_4 NPs/CGO/GCE bioelectrode for DNA hybridization with complementary, non-complementary and single base mismatch DNA sequence using MB as a redox indicator. Fig. 12 demonstrates the almost negligible changes of DPV signal, indicating no hybridization occurs. Furthermore, after hybridization with one base mismatch target DNA, nominal decrease is observed. This could be attributed to the mismatch formed at the proximal end. Since the mismatches that cause the unpaired at the end of the target strands to occupy more space than if they were hybridized, the proximal mismatch is restrained and is subject to stronger repulsions from the neighboring probe DNA sequences, therefore, the rate of the formation of the duplex and its stability is decreased [54]. While Large reduction in the magnitude of DPV peak current is observed, because of the hybridization with the complementary DNA sequence.

To evaluate the producibility and repeatability of the established biosensor, six times repeated experiments are conducted for complementary DNA sequences with the concentration of 10^{-10} M. The consequence of the relative standard deviation (RSD) with 3.9% is obtained, indicating the high capability of reproducibility of the developed DNA biosensor. The repeatability for each developed DNA biosensor is also surveyed, which is realized by immersing hybridized electrode into hot water (96℃) for 30 s to destroy the formed hydrogen bond between the double strand DNA. Subsequently, the regenerated biosensor is further committed to incubate with the target DNA sequences of solution of 10^{-10} M. The results reveal the regenerated bioelectrode can retain 93% (3 parallel experiments) signal efficiency after 2 times of regeneration compared to the original fabricated DNA biosensor.

A freshly constructed biosensor is stored for 2 weeks at 4 ℃ and further used to hybridize with the target ssDNA sequences, which achieves the retention of 91% (3 paralled experiments) of the initial signal response.

3.7 Evaluation in real samples

Table II. Detection of target DNA in real serum samples via the proposed biosensor.

Sample	Added (pM)	Found (pM)	Recovery (%)	RSD (%)
1	100	97.764	97.764	3.6
2	50	47.607	95.213	4.5
3	3	2.765	92.167	3.8
4	0.2	0.201	100.500	5.6
5	0.01	0.009	90.000	4.2

To assess the pratical specificity and affinity of the constructed DNA biosensor, as exhibited in table II, it was challenged with five human serum samples, which were diluted by ten fold and then added with various concentrations of target DNA(100 pM, 50 pM, 3 pM, 0.2 pM, 0.01 pM), it reveals

that the recoveries are ranging from 92.167% to 100.65% and the RSD are between 3.8% and 5.6%, proving the fabricated biosensor could still offer relatively accurate detection results despite of complex biological environment.

4. CONCLUSION

In this work, a simple, selective and highly sensitive DNA biosensor based on nanocomposite of Fe_3O_4 NPs/CGO is successfully proposed for the detection of Typhoidal Salmonella. The results manifest that the as-prepared nanocomposite offers more favorable sites for the immobilization of probe DNA and enhanced electron transfer rate. Under the optimized conditions, the fabricated DNA biosensor shows a wider linear detection range (1×10^{-17}-1×10^{-9} M) and a lower detection limit (3.16×10^{-18} M) for the target DNA than the DNA biosensors reported previously. It is also demonstrated that the ssDNA/Fe_3O_4 NPs/CGO/GCE bioelectrode possesses outstanding performance to distinguish between complementary, non complementary, one base mismatch DNA sequences. Significantly, we find that the bioelectrode indicates good analytical results when it is evaluated in real samples. Thus, this developed biosensor could potentially be applied to detect Typhoidal Salmonella in practice.

ACKNOWLEDGEMENTS
This work was supported by the National Natural Science Foundation of China (grant No.51772208) and (grant No.51678409) and Natural Science Foundation of Tianjin (No.07JCYBJC15900).

References

1. W. L. Cheng, C. W. Li, M. C. Li, N. Y. Lee, C. C. Lee, W. C. Ko, *J. Microbiol. Immunol. Infect.*, 49 (2016) 313.
2. P. Pashazadeh, A. Mokhtarzadeh, M. Hasanzadeh, M. Hejazi, M. Hashemi, M. D. L. Guardia, *Biosens. Bioelectron.*, 87 (2016) 1050.
3. N. T. V. Thieu, T. V. Tan, A. T. Tuan, E. J. Klemm, C. N. N. Minh, P. V. Vinh, D. P. Thanh, T. H. N. Dan, T. P. Duc, P. Langat, *J. Infect.*, 75 (2017) 104.
4. A. Karkey, T. Jombart, A. W. Walker, C. N. Thompson, A. Torres, S. Dongol, N. T. V. Thieu, D. P. Thanh, D. T. T. Ngoc, P. V. Vinh, *PLoS Neglected Trop. Dis.*, 10 (2016) e0004346.
5. S. Riti, C. Sanjay, R. H. Reed, *BMC Infect. Dis.*, 11 (2011) 1.
6. A. Singh, G. Sinsinbar, M. Choudhary, V. Kumar, R. Pasricha, H. N. Verma, S. P. Singh, K. Arora, *Sens. Actuators, B*, 185 (2013) 675.
7. M. Chen, C. Hou, D. Huo, M. Yang, H. Fa, *Appl. Surf. Sci.*, 364 (2016) 703.
8. L. Liu, X. Zhou, Y. Lu, D. Shan, B. Xu, M. He, H. Shi, Y. Qian, *Biosens. Bioelectron.*, 97 (2017) 16.
9. G. Rajeev, E. Xifre-Perez, B. P. Simon, A. J. Cowin, L. F. Marsal, N. H. Voelcker, *Sens. Actuators, B*, 257 (2017) 116.
10. L. Yuan, Y. M. Wang, W. Y. Zhu, C. H. Zhang, T. Hao, J. H. Jiang, *Anal. Chim. Acta*,1012 (2018) 60.
11. W. Wang, X. Hou, X. Li, C. Chen, X. Luo, *Anal. Chim. Acta*, 998(2018) 45.
12. Y. Ye, J. Xie, Y. Ye, X. Cao, H. Zheng, X. Xu, Q. Zhang, *Carbon*, 129 (2018) 730.

13. M. Chen, Y. Wang, H. Su, L. Mao, X. Jiang, T. Zhang, X. Dai, *Sens. Actuators, B*, 255 (2017) 2910.
14. J. Chen, Z. Liu, H. Peng, Y. Zheng, Z. Lin, A. Liu, W. Chen, X. Lin, *Biosens. Bioelectron.*, 98 (2017) 345.
15. M. Manzano, S. Viezzi, S. Mazerat, R. S. Marks, J. Vidic, *Biosens. Bioelectron.*, 100 (2017) 89.
16. F. Zhan, T. Wang, L. Iradukunda, J. Zhan, *Anal. Chim. Acta*, 1036 (2018) 153.
17. M. Chen, C. Hou, D. Huo, J. Bao, H. Fa, C. Shen, *Biosens. Bioelectron.*, 85 (2016) 684.
18. C. Jiang, T. Yang, K. Jiao, H. Gao, *Electrochim. Acta*, 53 (2008) 2917.
19. P. T. K. Loan, D. Wu, C. Ye, X. Li, V. T. Tra, Q. Wei, L. Fu, A. Yu, L. J. Li, C. T. Lin, *Biosens. Bioelectron.*, 99 (2018) 85.
20. E. Sharifi, A. Salimi, E. Shams, *Bioelectrochemistry*, 86 (2012) 9.
21. P. Liu, M. Zhang, S. Xie, S. Wang, W. Cheng, F. Cheng, *Sens. Actuators, B*, 253 (2017) 552.
22. B. Cai, S. Wang, L. Huang, Y. Ning, Z. Zhang, G. J. Zhang, *Acs Nano*, 8 (2014) 2632.
23. T. Dürkop, S. A. Getty, A. Enrique Cobas, M. S. Fuhrer, *Nano Lett.*, 4 (2004) 35.
24. R. R. Nair, P. Blake, A. N. Grigorenko, K. S. Novoselov, T. J. Booth, T. Stauber, N. M. R. Peres, A. K. Geim, *Science*, 320 (2008) 1308.
25. C. Lee, X. Wei, J. W. Kysar, J. Hone, *Science*, 321 (2008) 385.
26. D. Cheng, L. Yang, X. Li, J. Zhou, Q. Chen, S. Yan, N. Li, M. Chu, Y. Dong, Z. Xie, *J. Electrochem. Soc.*, 164 (2017) H345.
27. Y. Yoon, B. Lee Young, K. K. Seong, W. Song, S. M. yung, J. Lim, S. L. Sun, H. Yoo, K. S. An, *Chemistry Select*, 3 (2018) 321.
28. A. Bonanni, C. K. Chua, M. Pumera, *Chem. - Eur. J.*, 20 (2014) 2.
29. X. Sun, Z. Liu, K. Welsher, J. T. Robinson, *Nano Research*, 1 (2008) 203.
30. L. Yu, P. Li, X. Ding, Q. Zhang, *Talanta*, 165 (2017) 167.
31. X. Fan, W. Peng, Y. Li, X. Li, S. Wang, G. Zhang, F. Zhang, *Adv. Mater.*, 20 (2008) 4490.
32. X. Yang, X. Zhang, Y. Ma, Y. Huang, Y. Wang, Y. Chen, *J. Mater. Chem.*, 19 (2009) 2710.
33. A. Singh, M. Choudhary, M. P. Singh, H. N. Verma, S. P. Singh, K. Arora, *Bioelectrochemistry*, 105 (2015) 7.
34. W. S. H. Jr, R. E. Offeman, *J. Am. Chem. Soc.*, 80 (1958) 1339.
35. M. Peng, Y. Tang, W. Lei, *Acs Appl Mater Interfaces*, 9 (2017) 3940.
36. Q. Han, Z. Wang, J. Xia, S. Chen, X. Zhang, M. Ding, *Talanta*, 101 (2012) 388.
37. N. J. Kaleekkal, A. Thanigaivelan, D. Rana, D. Mohan, *Mater. Chem. Phys.*, 186 (2016) 146.
38. E. Er, H. Çelikkan, N. Erk, M. L. Aksu, *Electrochim. Acta*, 157 (2015) 252.
39. L. Huang, Y. Cao, D. Diao, Electrochim. *Acta*, 262 (2018) 173.
40. A. Lerf, ‡, H. He, A. M. Forster, J. Klinowski, *J. Phys. Chem. B*, 102 (1998) 4477.
41. S. Reddy, X. Xu, L. He, S. Ramakrishana, *Curr Opin Chem Eng*, 6 (2018) 120.
42. M. Chen, Y. Wang, H. Su, L. Mao, X. Jiang, T. Zhang, X. Dai, *Sens. Actuators, B*, 255 (2017) 2910.
43. Y. Yang, C. Li, L. Yin, M. Liu, Z. Wang, Y. Shu, G. Li, *ACS Appl. Mater. Interfaces*, 6 (2014) 7579.
44. K. Y. Goud, G. Catanante, A. Hayat, M. Satyanarayana, K. V. Gobi, J. L. Marty, *Sens. Actuators, B*, 235 (2016) 466.
45. J. E. B. Randles, *Trans. Faraday Soc*, 44 (1948) 322.
46. C. G. Xu, L. Y. Lan, Y. Yao, J. F. Ping, Y. B. Li, Y. B. Ying, *Sens. Actuators, B*, 273 (2018) 642.
47. M. Cui, Y. Wang, H. Wang, Y. Wu, X. Luo, *Sens. Actuators, B*, 244 (2017) 742.
48. M. Chen, C. Hou, D. Huo, H. Fa, Y. Zhao, C. Shen, *Sens. Actuators, B*, 239 (2017) 421.
49. W. Wang, T. Bao, X. Zeng, H. Xiong, W. Wen, X. Zhang, S. Wang, *Biosens. Bioelectron.*, 91 (2017) 183.
50. A. Sassolas, L. B. And, L. J. Blum, *Chem. Rev.*, 108 (2008) 109.
51. M. Díaz-Serrano, A. Rosado, J. Del Pilar, M. Arias, A. R. Guadalupe, *Electroanalysis*, 23 (2011) 1830.
52. T. M. Amouzadeh, M. Shamsipur, *Biosens. Bioelectron.*, 69 (2015) 100.

53. A. Singh, G. Sinsinbar, M. Choudhary, V. Kumar, R. Pasricha, H. N. Verma, S. P. Singh, K. Arora, *Sens. Actuators, B*, 185 (2013) 675.
54. E. Milkani, A. M. Khaing, S. Morais, C. R. Lambert, W. Grantmcgimpsey, *Anal. Methods*, 3 (2011) 122.